Toward an AlGaAs/AlOx near-infrared integrated optical parametric oscillator

C. Ozanam,[1] M. Savanier,[1] L. Lanco,[2] X. Lafosse,[2] G. Almuneau,[3] A. Andronico,[1]
I. Favero,[1] S. Ducci,[1] and G. Leo[1,*]

[1]*Université Paris Diderot, Sorbonne Paris Cité, Laboratoire Matériaux et Phénomènes Quantiques,
CNRS-UMR 7162, Case courrier 7021, 75205 Paris Cedex 13, France*
[2]*Laboratoire de Photonique et de Nanostructures, CNRS-UPR 20, Route de Nozay, 91460 Marcoussis, France*
[3]*CNRS, LAAS, Université de Toulouse, 7 avenue du Colonel Roche, F-31400 Toulouse, France*
*Corresponding author: giuseppe.leo@univ-paris-diderot.fr

We report on the observation of self-amplified parametric downconversion in a selectively oxidized AlGaAs cavity that was designed to perform as a guided-wave optical parametric oscillator in the near infrared. To date, two technological factors preclude such oscillation and are thoroughly investigated here: oxidation-induced optical propagation losses and the reflectivity of the waveguide resonator facets. The spectral study of the former has singled out two distinct mechanisms: scattering at the oxide interfaces and absorption by point defects in the oxide neighboring layers. Regarding the latter, dielectric mirrors have been designed and deposited on the ridge waveguide facets, with modal reflectivities of ∼10% at pump wavelength and ∼90% at signal/idler wavelengths. With respect to the case of a mirrorless waveguide, the monolithic cavity enabled a factor-2 enhancement of the conversion efficiency, indicating the close proximity of the oscillation threshold.   © 2014 Optical Society of America

OCIS codes: (130.7405) Wavelength conversion devices; (160.3130) Integrated optics materials; (190.4390) Nonlinear optics, integrated optics; (190.4410) Nonlinear optics, parametric processes; (310.2785) Guided wave applications.

http://dx.doi.org/10.1364/JOSAB.31.000542

1. INTRODUCTION

The optical parametric oscillator (OPO) is a broadly tunable optical source of coherent radiation [1]. Almost half a century after its former demonstration [2], this nonlinear device is not yet largely employed out of research contexts because its electrically pumped version is still lacking.

Unlike silicon and dielectric LiNbO$_3$, which are among the most popular materials of integrated photonics and nonlinear optics, respectively, direct-gap III–V semiconductors lend themselves to on-chip electrically injected nonlinear emitters. Among them, GaAs is likely to play a pivotal role in the near future, owing to its huge $\chi^{(2)}$ nonlinearity [$d_{36} \sim 100$ pm/V in the near infrared (IR)], its broad transparency window (from $\lambda \approx 0.9$ to 16 μm), and the mature fabrication technology borrowed from the microelectronics industry.

Among the phase-matching strategies that have been investigated so far in AlGaAs waveguides [3], form birefringence phase matching (FBPM) in AlGaAs/aluminum oxide (AlOx) waveguides has proved to be a viable option for the fabrication of frequency converters, thanks to their high efficiencies [4,5]. However, although AlOx technology is already established and used in the fabrication of vertical external-cavity surface-emitting lasers (VCSELs) both in academia and industry [6], its quality remains an issue for the most demanding photonic applications, where the photons have a strong overlap with the oxide.

Since the first demonstration of FBPM in AlOx waveguides [7], the optimization of their design and fabrication has

resulted in state-of-the-art performances for guided-wave $\chi^{(2)}$ interactions in AlGaAs [5,8]. For example, spontaneous parametric downconversion (SPDC) and parametric amplification have been demonstrated with normalized conversion efficiency $\eta_{\mathrm{norm}} \approx 1500\%$ W^{-1} cm^{-2} and a parametric gain coefficient of 4.1 cm^{-1} W$^{-1/2}$ [5,9].

Here we report on the observation of self-amplified SPDC in AlOx waveguides endowed with integrated mirrors, which constitutes significant progress toward the achievement of a waveguide OPO in the near IR. To reach this goal, two technological bottlenecks have been identified and addressed, namely (1) oxidation-induced distributed optical losses and (2) the reflectivity of the waveguide resonator facets.

This paper is therefore organized as follows: Section 2 is devoted to the SPDC nonlinear optical experiment in a waveguide cavity. The full study of the optical propagation losses in our AlGaAs/AlOx samples is then reported in Section 3. It aims at unraveling the mechanisms at their origin, in order to come up with solutions for a further improvement of the nonlinear performances. The design and fabrication of integrated mirrors are detailed in Section 4, as well as their characterization. Eventually, conclusions are drawn in Section 5.

2. GAAS/ALOX WAVEGUIDE CAVITY

A. Sample Fabrication

The structure that we consider here has been designed to operate as an OPO in the near IR, with degeneracy at 1.064 μm. It relies on a guided-wave type-I FBPM scheme
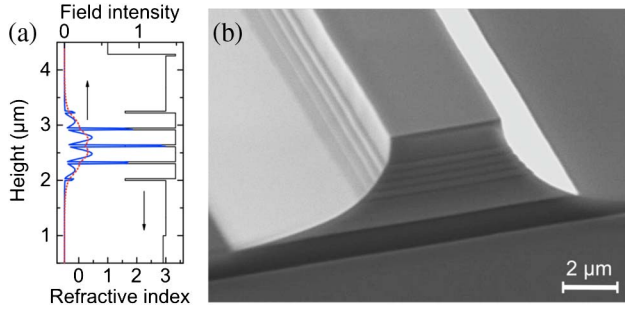
Fig. 1.   (a) Vertical index profile (thin solid line) and simulated phase-matched interacting modes at $\lambda_P = 1.064$ μm (solid blue line) and $\lambda_S = \lambda_I = 2.128$ nm (dotted red line). (b) SEM picture of a waveguide cleaved facet after oxidation.

between a TM_{00} pump mode at wavelength λ_P and two TE_{00} signal/idler modes at wavelengths λ_S and λ_I, respectively. The corresponding vertical layout, depicted in Fig. 1(a) along with the interacting mode profiles, consists of GaAs (substrate) / 1 μm $Al_{0.92}Ga_{0.08}As$ (spacer) / 1 μm $Al_{0.7}Ga_{0.3}As$ (bottom cladding) / $4 \times [37.5$ nm $Al_{0.98}Ga_{0.02}As / 273$ nm GaAs] / 37.5 nm $Al_{0.98}Ga_{0.02}As$ (core) / 1 μm $Al_{0.7}Ga_{0.3}As$ (top cladding) / 30 nm GaAs (protective cap). The design procedure was detailed in a previous communication [9].

This heterostructure has been grown by molecular beam epitaxy on a semi-insulating (001) GaAs substrate. Guiding ridges have been defined along the {110} crystalline axis by means of UV photolithography, then chemically etched with a $CH_3COOH:HBr:K_2Cr_2O_7$ solution, resulting in waveguides with extremely smooth sidewalls, as can be appreciated from the SEM picture given in Fig. 1(b). Typical waveguides are 3–4 μm wide, ~3 μm deep, and cleaved with a length of $L = 3$ mm. Eventually, $Al_{0.98}Ga_{0.02}As$ has been selectively transformed into AlOx by thermal wet oxidation. This process is performed in a tubular quartz oven at a temperature between 400°C and 450°C, exposing the waveguide sidewalls to an oxidizing gas stream [10]. In our setup, the latter is obtained by flowing dry N_2 (2L/min) through a water-filled bubbler heated at 70°C.

The practical realization of integrated mirrors on AlGaAs/AlOx waveguides is challenging in two respects: (1) it is important to preserve the cleanliness of the waveguide side-walls, as the slightest deterioration would entail scattering losses, and (2) due to $Al_{0.98}Ga_{0.02}As$ layers shrinkage during oxidation [11], the waveguide facets may be irregular and under mechanical stress. To this purpose, we have also developed a fabrication protocol that is presented in Section 4, along with the design procedure. It resulted in a 10% (resp., 90%) modal reflectivity for the pump mode (resp., signal and idler modes) around degeneracy.

B. SPDC Experiment

The SPDC experiment has been performed in 2 mm long waveguides with both end facets endowed with a dielectric Bragg mirror. This is the first SPDC measurement in an AlGaAs/AlOx integrated cavity.

To this end, the pump beam has been provided by a TE-polarized CW Ti:sapphire laser, tunable from 950 to 1100 nm, and a half-wave plate has been used to rotate its polarization to TM. This beam has been coupled into a waveguide through a ×60 microscope objective (0.85 NA)

mounted on a piezoelectric positioning system. At the output, an identical objective has been used to collect the IR beams, and the pump has been filtered out with a germanium window. The TE-polarized parametric fluorescence (PF) signal has been focused on an InGaAs photodiode, the photocurrent of which has been measured with a low-noise trans-impedance amplifier followed by a lock-in amplifier. Internal SPDC and pump powers, respectively P_{SPDC} and P_P, have been deduced after careful calibration of the experimental setup (with ~11% and ~7% uncertainties, respectively).

The P_{SPDC} versus P_P measurement is reported in Fig. 2. The data have been obtained for λ_P set at degeneracy, where parametric gain is the highest. In this case, type-I PM exhibits a huge spectral broadening, resulting in a maximum quantum noise effective input for the SPDC [12].

At moderate pump power, the SPDC power grows linearly (with an efficiency $\eta_{PF} = P_{SPDC}/P_P = 1.8 \times 10^{-7}$ W/W, which is lower than what we have reported for bare waveguides [5,8] due to smaller length and higher propagation losses). For $P_P \geq 75$ mW a marked superlinear trend becomes apparent, which reflects the fact that the nonlinear process goes unambiguously beyond the low-gain regime, close to the oscillation threshold (a similar observation was reported for periodically poled lithium niobate (PPLN) waveguides [13]). In this regime, the cavity mirrors recycle part of the signal/idler photons generated by SPDC. Parametric amplification occurs, and the IR radiation grows exponentially. The maximum pump power $P_P \approx 125$ mW coupled to the TM_{00} mode is obtained for ~300 mW focused on the entrance facet, which we found to be the maximum power that prevents irreversible damage of the coated facet in the permanent regime. Correspondingly, the P_{SPDC}/P_P ratio is enhanced by a factor of 2.1, without reaching the oscillation threshold, though. Plugging in the measured values of propagation losses ($\alpha_{S,I} \approx 1$ cm^{-1} and $\alpha_P \approx 3$ cm^{-1}) and modal reflectivity ($R_{S,I} = 90\%$) of the studied sample, we find that the OPO threshold should be reached for a pump power $P_P^{th} = 212$ mW (see Section 4). Although the oscillation threshold of the device is seemingly at reach, progress is still to be made in order to lower this value.
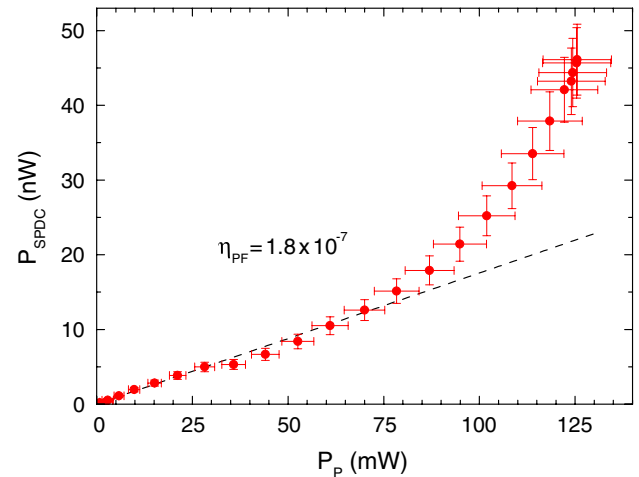

Fig. 2.   SPDC power versus pump power for λ_P set at degeneracy (red dots). At moderate pump power ($P_P \leq 75$ mW), $P_{SPDC} \propto P_P$ with an efficiency given by the slope of the linear fit (dashed line). The onset of parametric amplification at higher pump power suggests the proximity of the oscillation threshold.

To this end, specific efforts have been made concerning the amelioration of the nonlinear conversion efficiency, which can be achieved by two means: by reducing the optical propagation losses, and by improving the quality of the cavity mirrors.

3. OPTICAL PROPAGATION LOSSES

Optical propagation losses play a key role in all guided-wave phase-matching schemes, and their reduction is a critical issue. For this purpose, we optimized the thermal wet oxidation process using the feedback provided by systematic loss measurements. In addition, we investigated the possible loss mechanisms in order to single out specific technological limitations and initiate an adequate technological development.

After careful calibration of the oxidation apparatus, we confirmed that (1) the average loss level suffers from slow oxidation kinetics (i.e., from low temperature, since the reaction is thermally activated), and (2) the process must be stopped at the exact moment when the oxidation fronts merge at the center of the structure (i.e., when all the $Al_{0.98}Ga_{0.02}As$ has been converted into AlOx). In our case, the sample has been oxidized at 420°C for 14 min, which is our best trade-off between speed and reproducibility.

Despite this optimization, the present level of optical losses in such AlGaAs/AlOx waveguides is significant ($\alpha \sim 0.7$ to 1.5 cm^{-1} around $\lambda = 1.55$ µm) and hinders so far the demonstration of an integrated OPO with an acceptable oscillation threshold of the order of 100 mW. As a comparison, typical PPLN waveguide losses are in the range of few 0.01 cm^{-1}, enabling the fabrication of several centimeter-long OPOs with threshold as low as ~10 mW [13]. Thus, in order to develop a low-loss AlGaAs/AlOx waveguide technology, a better understanding of the optical loss mechanisms involved in such selectively oxidized AlGaAs devices is crucial.

Most of the propagation losses clearly originate from the oxidation process, as they are about three times lower before oxidation (~0.1 to 0.5 cm^{-1} around $\lambda = 1.55$ µm). However, the relevant loss mechanisms and their link with the AlOx properties remain uncertain. In particular, several aspects of the oxidation process are not yet clearly established, including the exact formation reactions and the fine chemical and structural properties of the oxide.

Thanks to a transmission electron microscopy (TEM) characterization of oxidized layers, carried out to assess the chemical and morphological properties of AlOx at the microscopic scale, it has been established that the oxidation process is responsible for the deterioration of the interfaces between layers [14]. In particular,

— AlOx layers are composed of γ-Al_2O_3 polycrystalline grains, sized between 10 and 20 nm, embedded in an amorphous Al_xO_y matrix,

— The roughness at AlGaAs/AlOx interfaces is increased by about 40% and 80% for GaAs and $Al_{0.7}Ga_{0.3}As$, respectively,

— Residual oxidation of the neighboring GaAs and $Al_{0.7}Ga_{0.3}As$ layers occurs through the interfaces over 3 and 9 nm, respectively,

— Further in the GaAs layers surrounding the AlOx, the material becomes amorphous in the vicinity of the oxidized layers (~20 nm from the interface) and remains monocrystalline beyond.

For high-index-contrast waveguides, optical losses are very sensitive to imperfections. We recall that the device dealt with here is passive; thus the semiconductor alloys have been chosen to be transparent at all the wavelengths involved in the $\chi^{(2)}$ process. In addition, in these waveguides operating in CW with internal pump powers $P_P \leq 125$ mW, the contribution of two-photon absorption (TPA) is not significant as α_{TPA} is ≤ 0.1 cm^{-1} [15]. Hence, assuming a good confinement, i.e., no optical leakage in the substrate by design, losses can only arise from scattering by rough interfaces or volume inhomogeneities, or from absorption by point defects.

Based on the above observations, our starting hypothesis was to ascribe the guided modes' propagation losses to scattering. However, the index contrast between AlOx and γ-Al_2O_3 being negligible, polycrystalline grains are not expected to contribute significantly to losses; thus we focused on the roughness of the (Al)GaAs/AlOx boundaries.

A. Empirical Model

The modeling of scattering losses in semiconductor waveguides is of considerable practical interest in the field of integrated optics. However, analytical solutions to this problem are not known, while brute-force FDTD numerical simulations do not constitute a practical option. Since Marcuse's pioneering work [16], a large amount of research has been done in this area, and most of the recent roughness studies in dielectric waveguides are based on the Payne and Lacey model [17]. This model provides a semi-analytical expression for the propagation losses of TE modes in low-index-contrast slab waveguides, in terms of waveguide parameters and statistical parameters of the rough interfaces, and it has been conveniently extended to the case of high-index-contrast semiconductor waveguides, for both TE and TM modes, by Schmid *et al.* [18].

Schmid's model deals with a symmetric slab waveguide with rough interfaces, as shown in Fig. 3(a). It provides the scattering contribution to the propagation losses by computing the radiated far field using a surface Green's function approach. Within this framework, and for a TE mode in a waveguide of thickness $2d$, the loss coefficient α_{TE} originating from scattering at the rough interfaces reads

$$\alpha_{TE} = \phi_y^2(d)(\Delta\varepsilon_r)^2 \frac{k_0^3}{4\pi n_{eff}}$$

$$\times \int_0^\pi [(1 + r_s(\theta))^2 + t_s^2(\theta)]\tilde{R}(\beta - n_2 k_0 \cos(\theta))d\theta, \quad (1)$$

where $\phi_y(d)$ is the normalized field intensity of the unperturbed mode at the interface, $\Delta\varepsilon_r = n_1^2 - n_2^2$ is the difference between the core and the cladding relative permittivities, k_0 is the free-space wavevector, $\beta = n_{eff} k_0$ is the modal propagation constant associated to the effective index n_{eff}, and r_s (resp., t_s) is the reflection (resp., transmission) Fresnel coefficient of a TE plane wave propagating at an angle θ with respect to the z axis. $\tilde{R}(k)$ is the Fourier transform of the autocorrelation function $R(u) = \langle f(z)f(z + u)\rangle$ of the profile $f(z)$ describing the interface roughness. It weighs the strength with which photons are scattered with an angle θ.

Let us note that a similar expression for TM-polarized modes exists, although it is somewhat more complex due to the discontinuities of the field $\phi_x(x)$ at the interfaces.
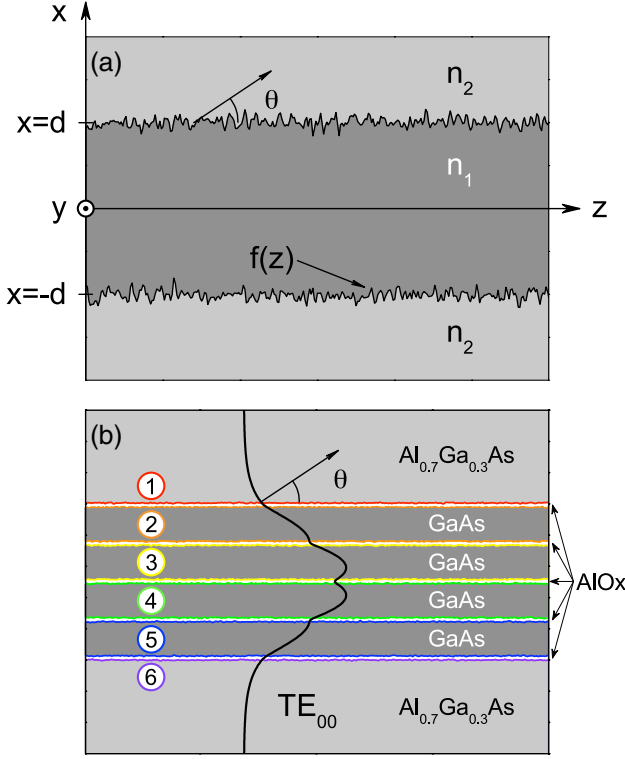
Fig. 3. Guided-wave scattering losses at rough interfaces. (a) Parameterization of the problem for a symmetric slab waveguide. (b) Adaptation to our multilayer AlGaAs/AlOx waveguide for the case of a fundamental TE mode.

Thus, the calculation of the scattering contribution to the waveguide losses requires the knowledge of the function $\tilde{R}$. In our case, for each type of interface within the waveguide, the corresponding autocorrelation function has been extracted from the TEM analysis mentioned above, and fitted with a Gaussian function [14]. The interfaces' roughness is therefore described by two statistical parameters: their root-mean-square deviation from the flat surface σ, and their correlation length L_C. The former is related to the autocorrelation function according to $R(0) = \sigma^2$, and the latter corresponds to the half-width at half-maximum of the Gaussian fit. The experimental values of σ and L_C estimated for the GaAs/AlOx and $Al_{0.7}Ga_{0.3}As$/AlOx interfaces of our waveguides are gathered in Table 1.

To qualitatively adapt Schmid's model to our multilayer structure, we split the waveguide into elementary vertical substructures. As shown in Fig. 3(b), the interfaces have been grouped into pairs to mark off regions with refractive index n_1 higher than the adjacent ones' n_2. The core of each guiding substructure, either GaAs or $Al_{0.7}Ga_{0.3}As$, sandwiched between AlOx layers, is numbered from 1 to 6. The fundamental TE mode can therefore be seen as a supermode resulting from the coupling of these six waveguides. To infer the

Table 1. Roughness Statistical Parameters of the AlGaAs/AlOx Waveguide Interfaces

Interface	σ (nm)	Δσ (nm)	L_C (nm)	ΔL_C (nm)
GaAs/AlOx	0.53	±0.08	53	±14
$Al_{0.7}Ga_{0.3}As$/AlOx	0.69	±0.08	30	±7

roughness-induced optical losses, we made the standard assumption that the roughness profiles are not correlated one to another, so that the contributions α_i ($i = 1, 6$) of each substructure add up incoherently:

$$\alpha_{TE}^{tot} = \sum_{i=1}^{6} \alpha_i. \tag{2}$$

The different terms of Eq. (2) have been computed thanks to Eq. (1), using the field intensity of the simulated TE_0 mode taken at each interface and the value of β calculated at the wavelength of interest, and by plugging in the adequate values of σ and L_C of Table 1. In addition, a factor 1/2 has been applied to α_1 and α_6 to account for the asymmetry of substructures no. 1 and no. 6 [18].

Let us stress that this adaptation can only result in a qualitative estimate, sufficient though to provide an order of magnitude estimate of the waveguide propagation losses. Since their spectral dependence is useful to discriminate between different loss mechanisms, this allows clarifying the spectral trend of the oxidation-induced roughness contribution. In this respect, while the roughness studies published to date largely focus on the influence of the waveguide geometry and confinement strength on losses [19,20], here we focus on assessing their wavelength dependence.

B. Experimental Results

The sample has been fabricated following the protocol described at the beginning of Section 2. Systematic loss measurements have been carried out on the best waveguides (typically five out of ~20) in order to evaluate the overall quality of the oxidized sample. Propagation losses before oxidation have been found to be 0.3 cm⁻¹ at $\lambda = 1.55$ μm. Regardless of the oxidation process, which remains the main source of sample deterioration, this low level of loss is ascribed to residual imperfections in the sample fabrication.

Among the different existing techniques to evaluate optical propagation losses, we opted for the Fabry–Perot fringes method [21], which is well suited for $\alpha \leq 1$ cm⁻¹ and only requires the knowledge of the modal reflectivity (estimated by 3D-FDTD simulations). However, for losses of several cm⁻¹, this technique is less reliable and we switched to transmission measurements. Let us recall that, unlike the Fabry–Perot technique, the accuracy of the latter also depends on the estimations of the coupling and collection efficiencies, which are calculated indirectly.

According to our FBPM scheme, we measured the losses of the TM_{00} mode (resp., TE_{00}) around 1.064 μm (resp., 2.128 μm). Around degeneracy, when the wavelength of the TM_{00} pump mode is tuned from 950 to 1060 nm, the TE_{00} signal wavelength ranges from 1060 to 2120 nm [22]. Accordingly, we used a set of linearly polarized CW lasers, tunable between 1280 and 1610 nm (*Tunics* telecom external cavity diode lasers), and around 2120 nm (*Nanoplus* DFB laser diode), for the Fabry–Perot fringe measurements, and between 950 and 1100 nm (*Spectra-Physics* Ti:sapphire laser) for the transmission measurements.

The experimental results are given in Fig. 4, along with the numerical results derived from the theoretical model presented in Subsection 3.A. The corresponding prediction band represents the set of curves obtained when σ and L_C are taken
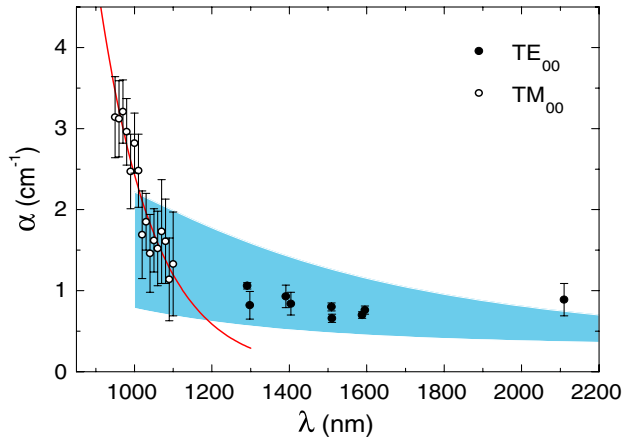
Fig. 4.   Propagation losses of the fundamental TM (circles) and TE (dots) modes versus wavelength λ. Below $\lambda \sim 1.1$ µm, data are fitted by a decaying exponential (red solid line). Above $\lambda \sim 1.1$ µm, the experimental data are bounded by the simulation results (blue stripe).

within the intervals $\sigma \pm \Delta\sigma$ and $L_C \pm \Delta L_C$ of Table 1. Since the waveguides are multimode, the Fabry–Perot method only provides us with an upper bound of the actual loss value [21]. Therefore, to avoid any overestimation of the propagation losses, the data reported at each wavelength correspond to the smallest of the five values obtained with the selected waveguides.

It appears that the error bars of the TM_{00} mode data are significantly bigger than their TE_{00} counterparts. As mentioned above, the transmission method is indeed less reliable than the Fabry–Perot one, so that the uncertainty is increased. Compared with the data acquired in the telecom band, the data at 2.12 µm also lack reliability and overestimate the actual loss value. This is due to the limited tunability of the laser diode ($\Delta\lambda \sim 1$ nm) used for this measurement, which does not allow us to refine this estimate based on the Fabry–Perot method.

Two different regimes can be clearly distinguished in Fig. 4:

— Above $\lambda \sim 1.1$ µm, losses are of the order of 1 cm^{-1} and decay as an inverse power law of the wavelength $\alpha \propto \lambda^{-N}$. According to the fits of the upper and lower bounds of the prediction band, we find $1.9 \leq N \leq 2.5$. The fair agreement between the experimental data and the model prediction confirms that in this spectral region, losses originate from scattering due to the AlOx layers' rough interfaces.

— Below $\lambda \sim 1.1$ µm, losses are much higher (up to 3 cm^{-1}) and exponentially diverge when λ decreases, thus clearly deviating from the prediction band.

C. Discussion

Very little literature addresses directly the study of optical losses in AlGaAs/AlOx devices beyond 1 µm. Let us mention, e.g., Ref. [23], in which an overall decreasing trend was observed for $\alpha(\lambda)$ of guided modes between $\lambda = 1.3$ and 2.1 µm. At shorter wavelengths, a few groups have reported huge levels of propagation losses around $\lambda = 775$ nm [4,24,25], but without an in-depth analysis. Although these features are similar to the ones reported here and seem inherent to AlOx-based devices, no systematic study of $\alpha(\lambda)$ has ever been carried out. This is why we thoroughly investigated

the propagation losses at all the wavelengths and for all polarizations involved in our SPDC process.

While the agreement between the experimental data and our simple scattering model is satisfactory for $\lambda > 1.1$ µm, the deviation observed at shorter wavelength points out the fact that our previous assumption is inadequate. Therefore, for $\lambda < 1.1$ µm, the sole scattering on surface imperfections is no longer sufficient to explain the propagation loss behavior, and a new loss mechanism, most likely accounting for bulk defects in the vicinity of the oxide layers, had to be considered.

As suggested by the high level of losses and their exponential decay with wavelength shown in Fig. 4, we opted for a model capable of describing absorption by defects at photon energies slightly smaller than the semiconductor bandgap, namely the Urbach's tail absorption model:

$$\alpha_{\mathrm{abs}} \propto \exp\left(\frac{E_{\mathrm{phot}}}{E_U}\right), \tag{3}$$

where $E_{\mathrm{phot}} = hc/\lambda \approx 1.24/\lambda$ is the photon energy [eV] at wavelength λ [µm], and E_U is the Urbach energy [eV] related to the absorption linewidth of the intragap localized state.

For $\lambda < 1.1$ µm the total losses are given by $\alpha = \alpha_0 + \alpha_{\mathrm{abs}} + \alpha_{\mathrm{scat}}$, where absorption ($\alpha_{\mathrm{abs}}$) and scattering ($\alpha_{\mathrm{scat}}$) contributions are added to the losses before oxidation (α_{NOX}). We therefore isolated α_{abs} by subtracting α_0 and the scattering baseline $\alpha_{\mathrm{scat}} = 5.28 \times 10^6 \; \lambda^{-2.2}$ from the raw data of Fig. 4. Its evolution with E_{phot} is given in Fig. 5, where the fit obtained from Eq. (3) with $E_U = 0.08 \pm 0.01$ eV is in qualitative agreement with the experimental data. Applying the same analysis to the data of Ref. [24], acquired in a similar AlGaAs/AlOx waveguide with degeneracy around $\lambda = 775$ nm, we found $E_U = 0.10 \pm 0.01$ eV. This value is comparable to the one reported here, suggesting that this high level of loss arises from the same type of defects in both devices.

The origin of this absorption is still unclear at the moment. Since Al_2O_3 and GaAs themselves are known to be transparent in the near IR [26,27], we tentatively ascribe these additional losses to point defects associated to energy levels in
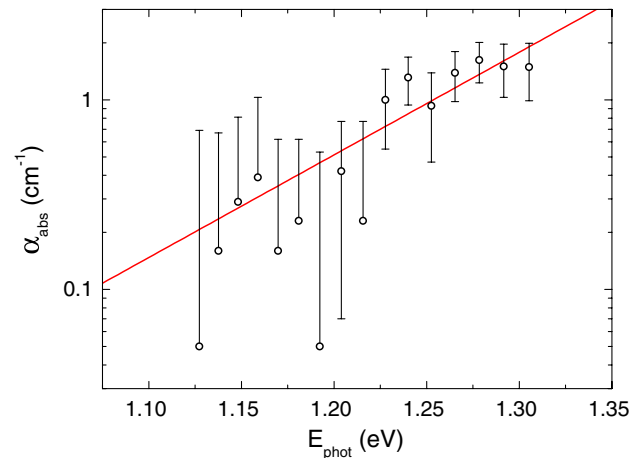

Fig. 5.   Absorption loss versus photon energy (semi-log representation). The experimental data (circles) are fitted with the exponential law $\alpha_{\mathrm{abs}} \propto \exp[E_{\mathrm{phot}}/0.08]$ (red solid line), compatibly with an Urbach's tail absorption regime.

the semiconductor gap, and created during the oxidation process in the GaAs layers adjacent to AlOx. Arsenic antisites (As_{Ga}) in particular have already been supposed to introduce donor levels with similar properties in the gap of AlGaAs, in optical devices [28] as well as in electrical devices [29]. Such defects may arise from trapped oxidation reaction products resulting in an excess of elemental arsenic As^0 at the oxide–semiconductor interfaces. Much As_{Ga} would then be generated after the diffusion of As^0 into the neighboring semiconductor layers [30], consistently with the TEM observations recalled at the beginning of this section [14].

Since propagation losses are currently the limiting factor for the demonstration of efficient integrated AlGaAs/AlOx devices, further minimization remains to be tackled. To this purpose four potential solutions are under study:

— Based on existing research on quantum-well luminescence close to oxidized layers, hydrogenation seems effective to remove absorbing species trapped at the oxide interfaces [31],

— Thermal annealing is also expected to diffuse defects out of the structure, and to restore the crystallinity of the amorphous materials,

— Shifting the coalescence of the counterpropagative oxidation fronts away from the center of the waveguide (i.e., where the fields are maximums) should prevent the formation of additional defects induced by over-oxidation [32].

— The insertion of thin lattice-matched GaInP barriers between the AlOx and GaAs layers seems effective to hamper the diffusion of As-rich oxidation reaction products into the latter, thus preventing the formation of point defects [33].

4. INTEGRATED OPTICAL CAVITY

Aside from decreasing the propagation losses, the other way to enhance nonlinear $\chi^{(2)}$ interactions consists in placing the parametric gain medium into an optical resonator [34]. As a consequence, the larger energy density resulting from intracavity light confinement enables us to trigger nonlinear processes with lower input powers and larger efficiency. This was demonstrated in III–V semiconductor devices such as the following:

— waveguides, where the implementation of Bragg mirrors has increased the brightness and the spectral purity of photon pair sources [35]

— microdisks, where the combination of high quality factors with good spatial overlap between the interacting whispering gallery modes has led to the demonstration of efficient second-harmonic generation (SHG) [36]

— photonic crystals, where low power SHG and optical bistability have been observed thanks to small mode volumes and high quality factors [37]

Beyond the increase of conversion efficiency, the positive feedback provided by an optical cavity is a prerequisite to reach the oscillation threshold of an OPO. In our case, the modest single-pass parametric gain of our AlGaAs/AlOx waveguides makes the quality of the cavity mirrors critically important toward the achievement of this goal. Quantitatively, the maximum parametric gain coefficient we can expect in a sample of length $L = 3$ mm with $\eta_{norm} \approx 1500\%$ W^{-1} cm^{-2} is $g = 1.3$ cm^{-1} for $P_P = 125$ mW (i.e., the maximum power we can safely couple into our waveguides) [7]. On the other hand, in addition to the typical signal/idler distributed propagation losses $\alpha \sim 1$ cm^{-1}, the concentrated mirror losses $\alpha_M = -1/2L \times \ln(R_1 R_2)$ are of the order of 0.3 cm^{-1} for reflectivities $R_i(i = 1, 2)$ as high as 91%.

A. Design of the Cavity
In view of the parametric oscillation, the choice of the cavity configuration has been made between the two practical optical resonators on which OPOs are mainly based, namely the singly resonant (SR) cavity and the doubly resonant (DR) one. In the first (resp., second) case, the cavity mirrors reflect only one (resp., both) of the signal/idler wavelengths. Since the pump threshold of the latter is typically one order of magnitude smaller than that of the former, we opted for a DR configuration, at the expense of a poorer spectral stability and tunability [1,12]. For a symmetric DR cavity with single pass of the pump, the steady-state pump power oscillation threshold P_P^{th}, which is minimum at degeneracy, reads [38]

$$P_P^{th} = \frac{1}{\eta_{norm}} \left[\frac{\alpha_P/2}{1 - \exp(-\alpha_P L/2)} \ln(R_{S,I} e^{-\alpha_{S,I} L}) \right]^2, \quad (4)$$

where α_P is the pump loss, $\alpha_{S,I}$ is the signal/idler loss, L is the waveguide length, and $R_{S,I}$ is the modal reflectivity at the signal/idler wavelength. We remind that for a phase-matched interaction in a lossy waveguide, η_{norm} is itself a function of L and α_j (its expression can be found in [12]). Plugging the experimental loss values of Subsection 3.B in Eq. (4), we find that for the pump threshold to be $\leq$100 mW, the mirrors' modal reflectivity at degeneracy should be $\geq$98% in a waveguide of optimal length $L \approx 2$ mm. Therefore, the nominal requirements of our mirrors were (1) a broad high-reflectivity (HR) stop-band centered about $\lambda = 2.12$ μm with $R_{max} = 99\%$, and (2) an antireflection (AR) window around $\lambda = 1.06$ μm with $R_{min} = 0.5\%$.

To meet these specifications, we opted for Bragg dielectric dichroic mirrors to be deposited onto waveguide facets. Their multilayer structure has been designed using the *Essential MacLeod* commercial software [39]. The widespread SiO_2/TiO_2 coating materials have been chosen for the bilayers of both mirrors, owing to their relatively high index contrast in the near IR ($\Delta n \sim 0.8$) that enables us to keep the thickness of the stack to a minimum. Six such bilayers turned out to be necessary to fulfill requirements.

B. Mirror Fabrication
The fabrication protocol that we have developed is based on ion beam assisted deposition (IAD) that enables the coating at relatively low temperature, hence avoiding annealing the sample, which could possibly alter the material quality. After oxidation, and prior to cleaving the sample facets, its surface is shielded from dielectric material overspray with a photoresist film (*Shipley S1828* baked at 120°C for 5 min) that is eventually stripped.

SEM pictures of waveguide facets taken at different stages of mirror fabrication are given in Fig. 6. As shown in Fig. 6(a), taken after the front-facet coating, the mirror (colored red) appears in the form of a dielectric "wall." A residual thin layer of overspray (colored yellow), under which the ridge shape is perceivable, is present on top of the sample. Figure 6(b)
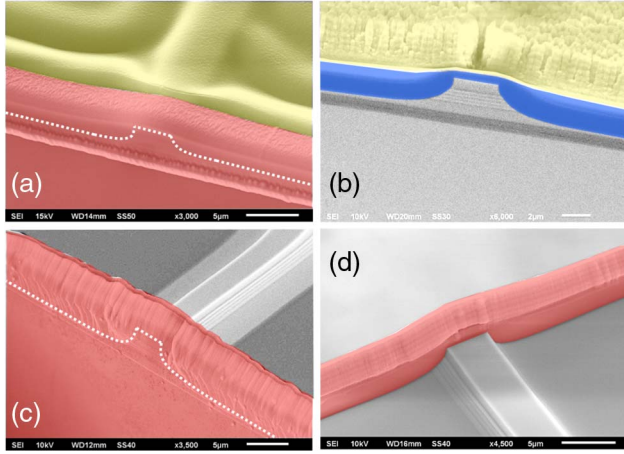
Fig. 6.   SEM bird's views of waveguide facets during the mirror fabrication process. (a) The coating materials form a plane mirror on the facet (red) as well as an overspray film on top of the sample (yellow). (b) The sample surface is shielded from overspray by the protective resist film (blue). (c), (d) Finalized mirror viewed from two different perspectives. The dotted line highlights the edge of the waveguide.
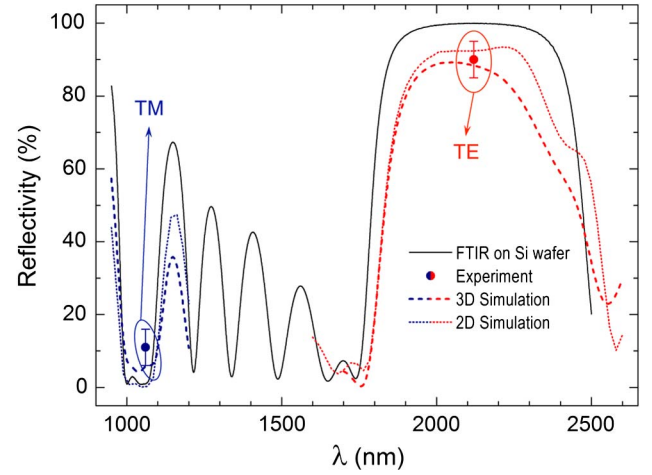

Fig. 7.   Experimental FTIR spectrum of a cavity mirror measured on a Si substrate (black solid line), measured modal reflectivities at $\lambda = 1.06$ μm for TM_{00} pump mode and $\lambda = 2.12$ μm for TE_{00} signal/idler modes (dots), and simulated guided-wave reflectivity spectra (dashed and dotted lines, respectively, for 3D and 2D calculations).

represents the freshly cleaved waveguide back facet, before coating. It provides a clear view of the overspray deposited at grazing incidence onto the protective resist layer (colored blue). After the second mirror deposition, the resist has been stripped and the overspray layer carefully removed. The overall quality of the mirrors and cleanliness of the sample surface can be appreciated in Figs. 6(c) and 6(d).

C. Optical Characterization
Besides the morphologic study of the fabricated cavities, we characterized them by measuring the mirrors' reflectivity.

In order to validate the multilayer design, a silicon wafer placed in the deposition chamber close to our sample and coated during the same run served as the control sample to check the reflectivity spectrum of one mirror. The related experimental Fourier transform IR (FTIR) spectrum is shown in Fig. 7, along with modal reflectivities measured at $\lambda = 1.06$ μm and $\lambda = 2.12$ μm, respectively, for the TM_{00} and TE_{00} modes. The former value has been inferred from a transmission measurement, resulting in $R_P = 11 \pm 5\%$. The latter has been inferred from the study of the Fabry–Perot fringes of a waveguide having one of its facets coated. A reflectivity $R_{S,I} = 90 \pm 5\%$ has been estimated from the finesse of the Airy function fitting the data.

While the FTIR spectrum meets the theoretical requirements in terms of AR at λ_P and broad HR stop-band at $\lambda_{S,I}$ around degeneracy, the measured modal reflectivities differ significantly from the target values. Such discrepancy is attributed to the 1D design procedure and the FTIR measurement, which only consider plane waves at normal incidence, while guided modes also experience diffraction losses at each reflection. As shown in Fig. 7, the experimental data are in better agreement with FDTD numerical calculations of the TM_{00} (resp., TE_{00}) mode reflectivity around $\lambda = 1.06$ μm (resp., 2.12 μm) accounting for this effect. Let us note that, even if the best agreement is obtained with accurate 3D-FDTD calculations, an acceptable alternative is obtained with the less time-consuming 2D-FDTD calculations (which only accounts for the vertical mode confinement).

As shown in Fig. 2, the feedback provided by our optical cavity enables the parametric self-amplification up to a factor 2 of the SPDC signal. Although the oscillation threshold has not been reached yet, this result reflects the technological progress achieved toward this ambitious goal. In order to lower the oscillation threshold to an acceptable value ~100 mW, we envisage to implement an asymmetric double pump-pass scheme, for which the back-facet mirror of the DR cavity is also highly reflective at λ_P. With respect to the present resonator configuration, a reduction of the pump power threshold by a factor 2–4 is expected, depending on the relative dephasing of the interacting modes after reflection upon the output mirror $\Delta\phi = \phi_P - \phi_S - \phi_I$ [40]. A drawback of this alternative is that the most favorable operating point along the frequency axis is not necessarily located at $\Delta k = 0$ (i.e., at exact phase-matching) but varies with $\Delta\phi$. Nevertheless, the value of $\Delta\phi$ can be controlled via a proper design of the multilayer output mirror [41], and λ_P could be conveniently used as a fine-tuning parameter to circumvent this problem.

5. CONCLUSION AND PERSPECTIVES
In this paper, we have reported the first observation of self-amplified SPDC in an AlGaAs/AlOx waveguide cavity. As a result of the Fabry–Perot effect due to the mirrors, an enhancement of the conversion efficiency up to a factor of 2.1 has been observed for pump powers ≥75 mW, suggesting the proximity of the oscillation threshold. Toward the demonstration of an optically pumped near-IR OPO based on such waveguides, two technological developments concerning the reduction of optical propagation losses, and the improvement of the quality of the integrated cavity mirrors, have been presented.

Subsequent to the optimization of the thermal wet oxidation process, valuable indications on the origin of the waveguide oxidation-induced deterioration have been provided by the measurement of optical propagation losses over a broad spectral range, ranging from 950 to 2120 nm, for both the TM_{00} and TE_{00} modes involved in the nonlinear process.

Two distinct loss mechanisms have been highlighted: (1) scattering at signal and idler wavelengths with $\alpha_{S,I} \approx 1$ cm^{-1}, due to the interface roughness between (Al)GaAs and AlOx layers, and (2) absorption at pump wavelength with $\alpha_P \approx 2–3$ cm^{-1}, due to volume defects in the semiconductor layers adjacent to AlOx.

Built-in dichroic mirrors have been designed and fabricated. The deposition of monolithic SiO$_2$/TiO$_2$ Bragg mirrors on the waveguide facets has led to a modal reflectivity $R_{S,I} \approx$ 90% in the stop-band around 2.12 μm, and $R_P \approx 10\%$ in the high-transmission window around 1.06 μm.

Despite the current waveguide optical losses, the AlGaAs/AlOx platform is very promising for photonic applications. Its further improvement will depend on a specific technological development of the oxidation process, along the lines discussed above. Beyond the demonstration of an integrated OPO, which seems now at reach, the insight in the loss mechanisms reported here for AlGaAs/AlOx waveguides can be of interest for a large number of optoelectronic devices.

ACKNOWLEDGMENTS

REFERENCES

1. M. Ebrahimzadeh and M. H. Dunn, "Optical parametric oscillators," in *OSA Handbook of Optics*, M. Bass, J. M. Enoch, E. W. Van Stryland, and W. L. Wolfe, eds. (McGraw-Hill, 2001), Vol. **IV**, pp. 22.1–22.72.
2. J. Giordmaine and R. Miller, "Tunable coherent parametric oscillation in LiNbO$_3$ at optical frequencies," Phys. Rev. Lett. **14**, 973–976 (1965).
3. A. S. Helmy, P. Abolghasem, J. Stewart Aitchison, B. J. Bijlani, J. Han, B. M. Holmes, D. C. Hutchings, U. Younis, and S. J. Wagner, "Recent advances in phase matching of second-order nonlinearities in monolithic semiconductor waveguides," Laser Photon. Rev. **5**, 272–286 (2011).
4. L. Scaccabarozzi, M. Fejer, Y. Huo, S. Fan, X. Yu, and J. Harris, "Enhanced second-harmonic generation in AlGaAs/Al$_x$O$_y$ tightly confining waveguides and resonant cavities," Opt. Lett. **31**, 3626–3628 (2006).
5. M. Ravaro, M. Le Dû, J.-P. Likforman, S. Ducci, V. Berger, G. Leo, and X. Marcadet, "Estimation of parametric gain in GaAs/AlOx waveguides by fluorescence and second harmonic generation measurements," Appl. Phys. Lett. **91**, 191110 (2007).
6. J. M. Dallesasse and D. G. Deppe, "III–V oxidation: discoveries and applications in vertical-cavity surface-emitting lasers," Proc. SPIE **101**, 2234–2242 (2013).
7. A. Fiore, V. Berger, E. Rosencher, P. Bravetti, and J. Nagle, "Phase matching using an isotropic nonlinear optical material," Nature **391**, 463–466 (1998).
8. A. De Rossi, V. Berger, M. Calligaro, G. Leo, V. Ortiz, and X. Marcadet, "Parametric fluorescence in oxidized aluminum gallium arsenide waveguides," Appl. Phys. Lett. **79**, 3758–3760 (2001).
9. E. Guillotel, M. Ravaro, F. Ghiglieno, C. Langlois, C. Ricolleau, S. Ducci, I. Favero, and G. Leo, "Parametric amplification in GaAs/AlOx waveguide," Appl. Phys. Lett. **94**, 171110 (2009).
10. K. Choquette, K. Geib, C. Ashby, R. Twesten, O. Blum, H. Hou, D. Follstaedt, B. Hammons, D. Mathes, and R. Hull, "Advances in selective wet oxidation of AlGaAs alloys," IEEE J. Sel. Top. Quantum Electron. **3**, 916–926 (1997).
11. O. Durand, F. Wyckzisk, J. Olivier, M. Magis, P. Galtier, A. De Rossi, M. Calligaro, V. Ortiz, V. Berger, G. Leo, and G. Assanto,

12. "Contraction of aluminum oxide thin layers in optical heterostructures," Appl. Phys. Lett. **83**, 2554–2556 (2003).
12. R. Sutherland, *Handbook of Nonlinear Optics* (Dekker, 2003).
13. G. Schreiber, D. Hofmann, W. Grundkoetter, Y. L. Lee, H. Suche, V. Quiring, R. Ricken, and W. Sohler, "Nonlinear integrated optical frequency converters with periodically poled Ti:LiNbO$_3$ waveguides," Proc. SPIE **4277**, 144–160 (2001).
14. E. Guillotel, C. Langlois, F. Ghiglieno, G. Leo, and C. Ricolleau, "TEM characterization of oxidized AlGaAs/AlAs nonlinear optical waveguides," J. Phys. D **43**, 385302 (2010).
15. W. C. Hurlbut, Y.-S. Lee, K. L. Vodopyanov, P. S. Kuo, and M. M. Fejer, "Multiphoton absorption and nonlinear refraction of GaAs in the mid-infrared," Opt. Lett. **32**, 668–670 (2007).
16. D. Marcuse, "Mode conversion caused by surface imperfections of a dielectric slab waveguide," Bell Syst. Tech. J. **48**, 3187–3215 (1969).
17. F. Payne and J. Lacey, "A theoretical analysis of scattering loss from planar optical waveguides," Opt. Quantum Electron. **26**, 977–986 (1994).
18. J. Schmid, A. Delâge, B. Lamontagne, J. Lapointe, S. Janz, P. Cheben, A. Densmore, P. Waldron, D.-X. Xu, and K. Yap, "Interference effect in scattering loss of high-index-contrast planar waveguides caused by boundary reflections," Opt. Lett. **33**, 1479–1481 (2008).
19. K. K. Lee, D. R. Lim, H.-C. Luan, A. Agarwal, J. Foresi, and L. C. Kimerling, "Effect of size and roughness on light transmission in a Si/SiO$_2$ waveguide: experiments and model," Appl. Phys. Lett. **77**, 1617–1619 (2000).
20. F. Grillot, L. Vivien, S. Laval, D. Pascal, and E. Cassan, "Size influence on the propagation loss induced by sidewall roughness in ultrasmall SOI waveguides," IEEE Photon. Technol. Lett. **16**, 1661–1663 (2004).
21. A. De Rossi, V. Ortiz, M. Calligaro, L. Lanco, S. Ducci, V. Berger, and I. Sagnes, "Measuring propagation loss in a multimode semiconductor waveguide," J. Appl. Phys. **97**, 073105 (2005).
22. M. Ravaro, E. Guillotel, M. L. Dû, C. Manquest, X. Marcadet, S. Ducci, V. Berger, and G. Leo, "Nonlinear measurement of midinfrared absorption in AlOx waveguides," Appl. Phys. Lett. **92**, 151111 (2008).
23. S. Venugopal Rao, K. Moutzouris, M. Ebrahimzadeh, A. De Rossi, G. Gintz, M. Calligaro, V. Ortiz, and V. Berger, "Influence of scattering and two-photon absorption on the optical loss in GaAs-Al$_2$O$_3$ nonlinear waveguides measured using femtosecond pulses," IEEE J. Quantum Electron. **39**, 478–486 (2003).
24. M. Savanier, A. Andronico, A. Lemaître, C. Manquest, I. Favero, S. Ducci, and G. Leo, "Nearly-degenerate three-wave mixing at 1.55 μm in oxidized AlGaAs waveguides," Opt. Express **19**, 22582–22587 (2011).
25. A. Fiore, S. Janz, L. Delobel, P. van der Meer, P. Bravetti, V. Berger, E. Rosencher, and J. Nagle, "Second-harmonic generation at λ = 1.6 μm in AlGaAs/Al$_2$O$_3$ waveguides using birefringence phase matching," Appl. Phys. Lett. **72**, 2942–2944 (1998).
26. J. R. Weber, A. Janotti, and C. G. V. de Walle, "Native defects in Al$_2$O$_3$ and their impact on III–V/Al$_2$O$_3$ metal-oxidesemiconductor-based devices," J. Appl. Phys. **109**, 033715 (2011).
27. M. A. Afromowitz, "Refractive index of Ga$_{1-x}$Al$_x$As," Solid State Commun. **15**, 59–63 (1974).
28. J. A. Kash, B. Pezeshki, F. Agahi, and N. A. Bojarczuk, "Recombination in GaAs at the AlAs oxide-GaAs interface," Appl. Phys. Lett. **67**, 2022–2024 (1995).
29. J. F. Chen, R. S. Hsiao, W. K. Hung, J. S. Wang, J. Y. Chi, H. C. Yu, and Y. K. Su, "Evolution of conduction and interface states of laterally wet-oxidized AlGaAs with oxidation time," J. Appl. Phys. **99**, 023711 (2006).
30. A. G. Baca and C. I. H. Ashby, *Fabrication of GaAs Devices* (Institution of Electrical Engineers, 2005).
31. S. Shi, E. Hu, J.-P. Zhang, Y.-L. Chang, P. Parikh, and U. Mishra, "Photoluminescence study of hydrogenated aluminum oxide-semiconductor interface," Appl. Phys. Lett. **70**, 1293–1295 (1997).
32. F. Chouchane, G. Almuneau, O. Gauthier-Lafaye, A. Monmayrant, A. Arnoult, G. Lacoste, and C. Fontaine, "Observation of overstrain in the coalescence zone of AlAs/AlOx oxidation fronts," Appl. Phys. Lett. **98**, 261921 (2011).

33. S.-C. Lee and W.-I. Lee, "$Ga_{0.5}In_{0.5}P$ barrier layer for wet oxidation of AlAs," Jpn. J. Appl. Phys. **39**, 2583–2584 (2000).
34. A. Andronico, X. Caillet, I. Favero, S. Ducci, V. Berger, and G. Leo, "Semiconductor microcavities for enhanced nonlinear optics interactions," J. Eur. Opt. Soc. **3**, 08030 (2008).
35. A. Orieux, X. Caillet, A. Lemaître, P. Filloux, I. Favero, G. Leo, and S. Ducci, "Efficient parametric generation of counterpropagating two-photon states," J. Opt. Soc. Am. B **28**, 45–51 (2011).
36. P. S. Kuo and G. S. Solomon, "Second-harmonic generation using 4-bar quasi-phasematching in a GaAs microdisk cavity," arXiv:1210.1984 (2012).
37. S. Buckley, M. Radulaski, K. Biermann, and J. Vučković, "Second harmonic generation in photonic crystal cavities in (111)-oriented GaAs," arXiv:1308.6051 (2013).
38. G. Bava, I. Montrosset, W. Sohler, and H. Suche, "Numerical modeling of $Ti:LiNbO_3$ integrated optical parametric oscillators," IEEE J. Quantum Electron. **23**, 42–51 (1987).
39. H. Macleod, *Thin-Film Optical Filters* (CRC Press, 2010).
40. J. E. Bjorkholm, A. Ashkin, and R. G. Smith, "Improvement of optical parametric oscillators by nonresonant pump reflection," IEEE J. Quantum Electron. **6**, 797–799 (1970).
41. V. Berger, "Second-harmonic generation in monolithic cavities," J. Opt. Soc. Am. B **14**, 1351–1360 (1997).